Mechatronics 98 (2024) 103117

Contents lists available at ScienceDirect

Mechatronics

journal homepage: www.elsevier.com/locate/mechatronics

An original hybrid-architecture finger mechanism for wearable hand exoskeletons☆

Chiara Brogi, Nicola Secciani, Lorenzo Bartalucci, Francesco Di Iorio, Enrico Meli, Mirko Rinchi, Benedetto Allotta, Alessandro Ridolfi *

Department of Industrial Engineering, University of Florence, Via di Santa Marta 3, 50139, Firenze, Italy

ARTICLE INFO

Keywords:
Wearable robotics
Assistive robotics
Hand exoskeletons
Hybrid architecture

ABSTRACT

Robotic devices for rehabilitation and assistance are becoming crucial tools for improving the life quality of people with disabilities. The hand is one of the most affected upper-limb parts, but also fundamental for the subject's interaction with the external environment. Wearability and portability, safety and comfort, lightness and small sizes, independent finger movement, efficacy in daily activities, sense-of-touch preservation, and affordability are the main features such devices should have. This paper will present an in-depth study of a thumb module for wearable hand exoskeletons, designed as a base concept to be adapted to the other fingers. Specifically, it exploits a new hybrid architecture (meaning that rigid and soft elements are included in the finger mechanism) to reduce the overall dimensions while remaining effective in force transmission. An embodiment of the mechanism is also presented and tested. As well as turning out to be small, light, and cheap, the new concept design demonstrates a minimum coverage of the finger range of motion of about 84% and an exerted force up to 16.78 N.

1. Introduction

The World Health Organization (WHO) declares that over one billion people suffer from some form of disability, and this number will increase due to a rise in chronic health conditions and population aging. In 2019, globally, 2.4 billion people with different impairments needed rehabilitation treatments to improve specific functionalities [1]. According to the WHO, about the same number of people should have benefited from rehabilitation at the end of 2021.

Among the others, hand function loss represents a limiting disability that can have numerous causes and affect people of all ages. Increasing age, unhealthy eating habits, decreasing physical activity or visual acuity, and more severe diseases such as diabetes, stroke, Parkinson's, senile dementia, and tremor may negatively impact hand capabilities [2] and even lead to complete hand dysfunction [3]. Hand impairments are also expected at a younger age, e.g., due to traumas or congenital disorders [4]. The hand is a sophisticated tool that enables humans to interact with the surrounding environment with extreme flexibility: touching, manipulating, grasping, holding, tightening, feeling, and communicating are only some activities performed by combining the different hand functions [5–8]. Hand dexterity allows for many Activities of Daily Living (ADLs) at home, school, and work. Also, hands are crucial in interpersonal relationships. All these characteristics make the hand a challenging research topic. From an engineering perspective, current development trends are pushing research activities to investigate two main topics: robot-assisted rehabilitation and robotic assistance.

Robot-assisted rehabilitation is a set of innovative methods that enable accurate, highly repetitive, intensive, and adaptive to patient's performance and needs treatments by exploiting end-effector or exoskeleton robots [8–12]. Such devices can measure several parameters, e.g., subjective performance, spasticity, reflexes, and functional movements, to track and analyze rehabilitation patterns and progress made, and be remotely controlled, enabling therapists to treat patients more efficiently, thus reducing their effort, time, and cost [13–15]. As well as rehabilitation robots for clinical settings [9,10,16–19] – some of which are already commercially available, e.g., *Gloreha* from Idrogenet or *InMotion ARM* from Bionick – a first generation of devices designed for different environments (e.g., at home or for virtual reality) has come out as a more-engaging alternative [20–27]. Despite promising results, robot-assisted rehabilitation is still an open research topic [10]. Robot-assisted therapy is not necessarily more effective than the conventional one in terms of recovering motor functions, control, strengths, and improving ADLs performance as the patient itself, its recovery stage, the device used, and treatment intensity and duration may influence

☆ This paper was recommended for publication by Associate Editor Sinan Haliyo.

* Corresponding author.
E-mail address: alessandro.ridolfi@unifi.it (A. Ridolfi).

https://doi.org/10.1016/j.mechatronics.2023.103117
Received 6 March 2023; Received in revised form 26 October 2023; Accepted 5 December 2023
Available online 21 December 2023

the outcomes [11–13,28,29]. Conversely, assistive devices [30–43] are designed to help users in everyday activities, overcoming their impairments. They must be lightweight, wearable, portable, force effective, and correctly coupled with the hand to avoid wrong and painful poses [8,44–46]. Nowadays, the distinction between assistive and rehabilitative exoskeletons is not always clear-cut since some of the rehabilitation devices are also thought for home-based treatments [20–24,26,30,31,33,39,43] and, for this reason, might also be used as constrained assistance tools.

Different aims result in different mechanical architectures: from this point of view, Hand Exoskeleton Systems (HESs) can be classified as soft or rigid. Soft architectures, such as cable-driven gloves [35,36,38,40], and fiber-reinforced [21], polymer-or-elastomer-based [33], fabric-based [34] solutions, are preferable in wearable devices to reduce weight and dimensions and increase compliance, comfort, and portability [39,47]. Nevertheless, they are helpful only for low assistance levels due to the forces they can exert. High forces and accuracy are, instead, crucial features of rigid architectures (e.g., linkage-based mechanisms [20,23,24,26,30–32,42,43,48–53]), which, conversely, present low compliance and could lead to wrong motions if not correctly coupled with the hand [44]. Besides, linkage-based architectures usually result in cumbersome systems that are hardly exploitable in confined spaces or for fine manipulations. In recent years, first hybrid solutions, i.e., including both rigid and soft elements in their mechanical structure, were studied [22,36,39], and the presentation of one of these last represents the main topic of this manuscript.

The main contribution of this paper is to present an original design for a finger exoskeleton exploiting a hybrid mechanical architecture for driving the finger flexion/extension (f/e) motion as the base concept for an assistive wearable hand exoskeleton. The HES prototype recently developed by the Mechatronics and Dynamic Modeling Laboratory (MDM Lab) of the University of Florence (UNIFI) [42] still had some drawbacks to this aim. Even if the kinematic structure [54] and the myoelectric control strategy [55,56] are crucial strengths of this device, the weight on the hand back, overall dimensions, and bulky mechanisms on the fingers limit its usage for delicate and in-confined-space manipulation tasks. Equipped with just one motor to prevent the remote placement of components, such a HES does not allow for independent finger movement, which is a feature that significantly affects tip and tripod grasp [57], while the lack of the thumb actuation represents another critical flaw of the device. Starting from these considerations, the paper proposes the conceptualization and a first prototyping of a new device designed to overcome the issues mentioned above (i.e., bulkiness, forcibly simultaneous finger motion, and thumb module lack) while remaining fully wearable and exerting forces suitable for ADLs. All of the above requirements will be detailed later in the article.

The proposed hybrid architecture is described for the thumb but can be easily adapted to all the other fingers to develop a fully wearable and portable assistive hand exoskeleton. Such a solution was born to merge soft and rigid architectures to achieve a lightweight and force-effective mechanism that is also usable in confined spaces. Unlike other devices available in the literature, the proposed design relies the actuation of the MetaCarpoPhalangeal (MCP) joint on a well-known rigid architecture while delegating that of the other finger joints to a particular soft architecture. The design started with accurate kinematic and kinetostatic analyses; then, it was validated through simulation and practical tests on the achievable *Range Of Motion* (ROM) and exerted forces. Overall, the article provides a detailed example of the design procedure (from concept to preliminary operational testing) of a wearable robotic system for assistive use, showing the development of a hybrid thumb mechanism that will represent the basis for the design of the whole HES.

The paper is organized as follows. Section 2 shows the Material and Methods for the study, including a brief description of the thumb anatomy, the design choices related to the main requirements for wearable hand exoskeleton for assistance, the mechanism synthesis and embodiment. Section 3 reports some preliminary tests and achieved results regarding the mechanism ROM and exerted forces, subsequently discussed in Section 4. Section 5 will conclude the paper.

Table 1
Range of thumb joint angles [58].

Joint angular coordinates	Maximum flexion	Maximum extension
θ_{MCP} [°]	60	10
θ_{IP} [°]	90	20

2. Material and methods

2.1. Overview on the thumb anatomy

As well as the carpal and metacarpal bone, the thumb has two phalanges: the proximal and distal ones. Joints among these bones enable them to move; specifically: (i) the MCP joint stands between the metacarpal and proximal phalanx, (ii) the InterPhalangeal (IP) joint stands between the proximal and distal phalanges. The MCP joint enables the proximal phalanx f/e and abduction/adduction (a/a) movements, while the IP joint has just one Degree of Freedom (DoF), allowing the distal phalanx f/e motion.

In this work, joints trajectory was identified by exploiting a hand kinematic model available in the literature [58,59]. The finger is modeled as a rigid kinematic chain whose joints and links correspond to finger joints and bones. The Denavit-Hartenberg (D-H) method was applied to the thumb kinematic chain to determine the IP joint and fingertip position and orientation, namely its pose, related to a reference frame centered in the MCP joint, as the following dissertation required. The MCP a/a is neglected as the finger mechanism will only actuate the thumb phalanges f/e motion. The MCP and IP joint angular coordinates are considered to span as reported in Table 1.

2.2. Design choices for a hand assistive device

An interesting explorative interview conducted to understand what end-users and clinicians expect from an assistive hand exoskeleton [46] revealed that these devices should assist all the fingers and help the patient during desired activities thanks to an intuitive control strategy and, as long as possible, considering its battery life and comfort, should allow wrist motion, exert forces to lift at least a drink, and have small dimensions and weight, which should not exceed 200 g on the hand. Although this preliminary study should be carried out on a larger participants sample, the obtained results agree with many reviews in the literature [8,44,45,47,60]. Specifically, the main requirements for assistive hand exoskeletons are:

(1) *Wearability and portability:* HES should be limited in dimensions and weight to achieve these aims and not constrained by remotely-located components [60], which limit the patient mobility as well as the device portability;
(2) *Safety and comfort:* hand exoskeletons must ensure patient safety and comfort over prolonged use. Customized devices are preferred; also, the HES must be correctly coupled with the hand and its mechanisms aligned with the fingers to avoid wrong or excessive movements that may cause pain to the user;
(3) *Lightness and small size:* they are crucial requirements for assistive hand exoskeletons, as all those mentioned above depend on them. HESs should not exceed the limb dimensions and weigh more than 200 g on the hand back and more than 500 g on the forearm [46];
(4) *Independent finger movement:* it guarantees a more natural experience than coupled-finger solutions and helps grasp irregular-shaped objects [57];

(5) *Efficacy in ADLs:* since the HES's primary purpose is to assist in ADLs or eventually to perform at-home rehabilitation, it should be able to exert suitable forces for typical everyday life activities; the target force chosen is 15 N per finger, as a value in accordance with other experimental research in the literature [61,62]. In the ideal case in which the object weight is equally distributed over the fingers, and considering an average friction coefficient of 0.3 for ordinary objects of daily living (e.g., a ceramic mug, plastic bottle, wooden hair brush, metal scissors), the target amount of force per finger shall make it possible to lift objects weighing up to 2.3 kg, which is a slightly higher value than the average of daily objects [63];
(6) *Sense-of-touch preservation*: as tactile sensations are crucial feedback, the HES should not foreclose the touching objects but preserve as much of the natural sense of touch as possible;
(7) *Affordability:* as one of the aims for which Robotics for Medicine and Healthcare was born, robotic devices should democratize treatments and be affordable for those in need.

In light of these reasons, the new hand exoskeleton design concept was defined. The device was conceived with all the components integrated on the hand and forearm to improve the overall weight distribution while avoiding remote components to boost both *wearability* and *portability* [60]: specifically, five independent finger modules mounted on the hand back, and a box fixed to the forearm that contains the control and power supply units compose the exoskeleton. The finger modules (the thumb one mounted on a hand model is shown in Fig. 1) were designed to include a hybrid architecture as finger-handling mechanism to achieve *small overall dimensions* by involving soft elements, thus ensuring usage in confined spaces, and *efficacy in ADLs* thanks to exploiting also a rigid structure. This new architecture replaced the bulkier single-phalanx, linkage-based, and cable-driven mechanism exploited in the previous HES version [42]. The linkage-based mechanism was designed to exert a normal force of 15 N on the middle of the proximal phalanx, ensuring suitable *efficacy in ADLs*. At the same time, soft elements have to guarantee complete distal phalanx f/e. Each rigid mechanism must be correctly aligned with the corresponding finger to achieve a safe and comfortable device: for this reason, a 1-DoF Remote Center of Motion (RCM) mechanism [64,65] was designed to match the natural MCP joint of each finger [44]. There are several kinds of 1-DoF RCM mechanisms (e.g., circular-prismatic-joint [18,23,30,31], parallelogram-based [16,49], double-parallelogram-based [26,66], four-bar mechanism [32]). Also multi-DoF mechanisms should be considered since there is no need to align the finger and mechanism before use while increasing the mechanism's overall dimensions and complexity [48]. In this work, precisely a four-bar mechanism (involving the proximal phalanx as a "bar") was exploited as it allows its RCM to coincide easily with the MCP joint [67]. Moreover, the well-known four-bar mechanism kinematics lends itself well to an optimization procedure proposed in [68] and revised for this configuration. This last characteristic allows for quick and easy mechanism customization on the specific user's hand size, which is fundamental for device *safety* and *comfort*. As regards the soft part, similarly to [39,69], flat springs were exploited to actuate the distal phalanx f/e movement. Springs were assembled to achieve the maximum possible ROM for the IP joint (DIP one for the other fingers) by sliding through the end-effectors of the rigid and soft architectures, respectively yellow-and-blue colored in Fig. 1. It is worth noting that soft elements automatically align with the finger due to their flexible nature. The four-bar mechanism, instead, is correctly aligned with the finger when its RCM coincides with the MCP joint, and the mechanism end-effector corresponds to the middle of the proximal phalanx, thus establishing a safe and comfortable interaction with the finger itself. This implies that an optimization procedure is crucial to achieving such a kinematic correspondence between the mechanism and the finger.

Besides the mechanical architecture, the type of actuators is a fundamental factor in designing any device as it can affect its wearability and portability: different types of actuation can be employed in wearable robotic systems, and each grants unique features to the system. Pneumatic and hydraulic actuators are commonly exploited in soft wearable devices, especially with polymer-or-fabric-based and fiber-reinforced structures, such as artificial muscles, bending, or cylinder actuators. Even though hydraulic actuators have higher power density and efficiency than pneumatic ones [8,70], the two types can exert suitable forces for ADLs, but their portability is generally worse than electric motors [44,70]. Indeed, pneumatic and hydraulic actuators need a pump, valves, and channels connected to the actuators, in addition to the control electronics and battery pack, while the hydraulic ones also require a water reservoir. As a result, the weight of the systems can be very high, and the actuation and control units must necessarily be dislocated [8,21,33,34]. In addition, possible leakages confine their use to a not-so-large niche of applications as they may compromise the device safety. Electric actuators (the other big family) are usually preferred for wearable applications [60]. This condition is probably due to their high portability, safety, reliability, and ease of control. Several models of as many weights, sizes, and power outputs are available on the market. In this context, the usage of electric actuators was confirmed (for *wearability*, *portability*, and *safety*), but the single servomotor of the previous version was replaced with five micro gearmotors, one per finger, thus providing the HES with *independent finger movement*. The actuator model (see Section 2.4 for more detail) was selected, bearing in mind the 15-N target force to be exerted in the middle of the proximal phalanx for *efficacy in ADLs*.

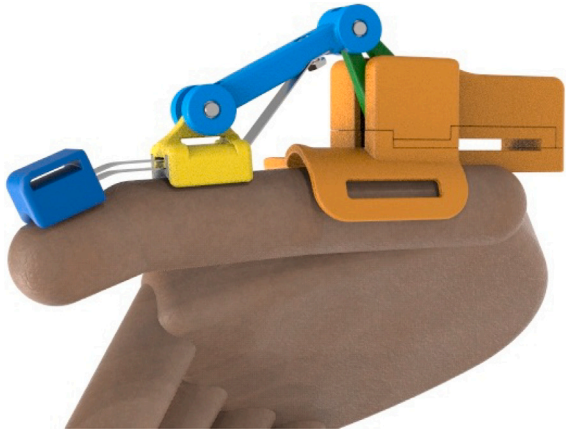

Fig. 1. An overview of the hybrid-architecture finger exoskeleton proposed in this work.

Even the transmission system can influence the device's safety and comfort. Flexible solutions, such as cable transmissions, are commonly used with electric motors [70] for soft architectures (acting as tendon systems [35,38,40]) and rigid ones [24,42]. One of the most used solutions consists of electric motors placed in a remote location actuating Bowden cables connected to the HES for transmission [21,22,32,35,36,39,49,51,52]. They are compliant and light, ensuring comfort; however, cable-driven exoskeletons suffer from loss problems and non-linear tension variation due to friction and backlash [70]. Besides, bidirectional motion is allowed only by specific cable configurations (e.g., pull-pull configuration), which increases overall dimensions and complexity, reducing wearability and portability [70,71]. Even rigid solutions, such as gears or linkages, are usually combined with electric motors [23,30,37,43,48,50,53] and can transfer forces without losses, but they need to be highly accurate from a kinematic point of view [9,70]. Exploiting a flexible shaft between rigid elements is a trade-off solution [72] initially chosen for this work. Indeed, firstly, it would have enabled moving the actuation and control systems away from the hand, improving mass distribution, and, secondly, it could have transmitted torque more efficiently than Bowden cables. However, the

Table 2
Main features of state-of-the-art devices for assistance or at-home rehabilitation.

References	Fingers	Independent finger movement	Transmission system	Actuators	Mechanism architecture	Forces [N]	Weight on the hand/total [g]	Alignment	Remote location
Lambercy et al. (2013) [20]	T	–	Rigid linkage	Linear motor	Linkage mechanism (R)	2–10	126/–	Yes	Yes
Polygerinos et al. (2015) [21]	All	No	–	Hydraulic	Fiber-reinforced elastomeric chambers (S)	8	285/3300	Yes (Auto)	Yes
Randazzo et al. (2017) [22]	All	T, I, M, R-S	Bowden cables	Linear motors	Rigid sheath guides and cables (H)	5	50/930	Yes (Auto)	Yes
Wang et al. (2018) [23]	All	T, I-M-R-S	Linkage mechanism	DC motors	Linkage mechanism (R)	–	420/420	Yes (Circular-prismatic joint)	No
Bouteraa et al. (2019) [24]	All	Yes	Cables	Servomo-tors	Linkage based (R)	–	388/388	Yes	No
Sandison et al. (2020) [26]	All	Yes	Rigid linkage	Linear motors	Linkage mechanism (R)	–	340/340	Yes (Double-parallelogram mechanism)	No
Yun et al. (2017) [32]	T, I, M	Yes	Bowden cables	Electric motors	Linkage mechanism (R)	–	205/–	Yes (4-bar mechanism)	Yes
Ang et al. (2017) [33]	All	No	–	Pneumatic	Elastomer based (S)	41,8 (Grip)	–/1500	Yes (Auto)	Yes
Cappello et al. (2018) [34]	All	No	–	Pneumatic	Fabric-based glove (S)	15 (Grasp)	77/5000	Yes (Auto)	Yes
In et al. (2015) [35]	T, I, M	T, I-M	Bowden cables	Rotational motor	Glove (S)	9-12	194/–	Yes (Auto)	Yes
Rose et al. (2018) [36]	All	T, I, M-R-S	Bowden cables	DC motors	Rigid elements, glove (H)	16,6 (Grasp)	220/16000	Yes (Auto)	Yes
Zhao et al. (2020) [37]	All	T, I-M-R-S	Linkage mechanism	Linear motors	Linkage mechanism (R)	9	/183	Yes	–
Yurkewich et al. (2020) [38]	All	No	Cables	Linear motors	Glove (S)	–	377/377	Yes (Auto)	No
Dittli et al. (2020) [39]	All	T, I-M-R-S	Bowden cables and gears	DC motors	Three-layered springs, rigid elements (H)	–	259/560	Yes (Auto)	Yes
Popov et al. (2016) [40]	T, I, M, R	Yes	Cables	DC motors	Glove (S)	16 (Pinch)	250/340	Yes (Auto)	No
Secciani et al. (2021) [42]	I, M, R, S	No	Cables	DC motors	Linkage mechanism	–	460/540	Yes	No
Esposito et al. (2022) [43]	I, M, R, S	No	Gears and linkages	Servomo-tor	Linkage mechanism (R)	94 (Grasp)	380/500	No	No
Sarakoglou et al. (2016) [48]	T, I, M, R	Yes	Gears	DC motors	Linkage mechanism (R)	4.8	–	Yes	No
Li et al. (2022) [53]	T	–	Linkage mechanism	DC motors	Linkage based (R)	12	206/–	Yes	–

stringent dimensional constraints prevented exploiting this attractive component as commercially available flexible shafts could not fit (one per finger) on the hand back, and a gear transmission was chosen, thus improving *safety* through its kinematic accuracy, and enabling the active finger opening and closing without increasing the device overall dimensions. Last but not least, Velcro straps will connect the end-effectors and fingers and fix the exoskeleton to the hand to leave the hand palm as accessible as possible, thus ensuring better *sense-of-touch preservation* than gloves usage. Finally, the mechanism bars and other rigid parts will be 3D printed in Acrylonitrile Butadiene Styrene (ABS), ensuring *lightness* and greater *affordability* compared to standard industrial production.

A careful investigation of the current state of the art was conducted to justify and better understand the choices made to meet the above-mentioned requirements. Table 2 highlights the main features of the most interesting existing solutions. Specifically, the table summarizes which fingers are actuated (they are denoted as follows: T = Thumb, I = Index, M = Middle, R = Ring, S = Small), if the system enables the independent finger movement (if not, the symbol (–) will be found between the coupled fingers), the transmission and actuation systems exploited, the mechanical architecture of the system (S = Soft, R = Rigid, H = Hybrid), the exerted forces, the weight on the hand or remotely placed, if and, eventually, how the alignment issue is considered, and finally if some components are remotely located. The exerted force values are reported and matched with the corresponding action in brackets, if declared. Concerning the alignment issue, it is worth noting that soft structures automatically align to the hand, and this aspect is highlighted by the string "(Auto)". Finally, the symbol (–) means that the matching information is not reported in the article.

The data reported in the table highlights these considerations. As expected, pneumatic and hydraulic actuators are heavy; thus, they are placed in a remote location from the hand [21,33,34]: this solution lightens the hand but reduces the freedom of patient movements [60]. It follows that, from an assistive point of view, placing the actuation

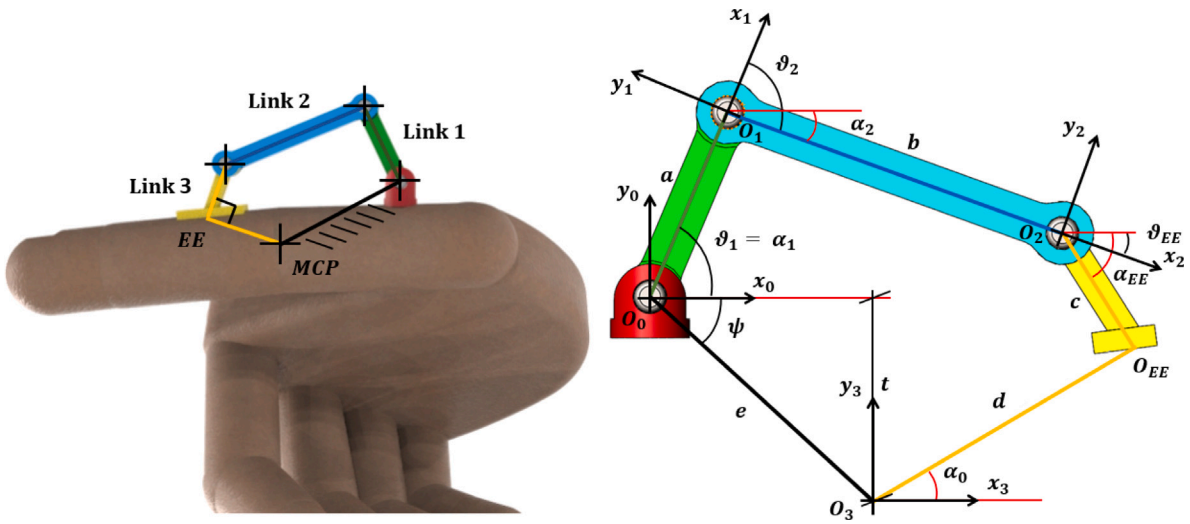

Fig. 2. On the left, the schematic four-bar mechanism placed on the thumb of a hand parametric CAD model is shown. Its bars are highlighted: (i) the mechanism frame, black colored, (ii) Link 1, green colored, (iii) Link 2, blue colored, and (iv) the third bar, consisting of the rigid mechanism Link 3 and part of the proximal phalanx, yellow colored. In addition, the MCP joint (O_3) and EE are shown. On the right, the reference frames convention for kinematic analysis is reported.

and control units close to the hand is preferable. Finger modules and actuators can be placed on the hand back, and control units on the forearm to better distribute masses and reduce user fatigue [26,38]. Some solutions exploit linear DC motors [20,22,26,37,38]; however, they result slower and bulkier than rotational ones.

2.3. Mechanism synthesis

This section will deepen the kinematic synthesis of the new hybrid finger mechanism [73]. Specifically, the thumb module will be addressed since it was lacking in the previous MDM Lab prototype [42]. Only the f/e movement was considered in this study, and it can be easily generalized to the other fingers by adapting the mechanism to different dimensions. The CMC joint circumduction and opposition motions are left to further investigations.

2.3.1. The rigid architecture

As reported in Section 2.2, the mechanism rigid architecture was designed to act on the middle of the proximal phalanx using a four-bar mechanism, including some hand parts as the "bars", as visible on the left in Fig. 2. In this configuration, the mechanism end-effector (schematized as the point EE for the kinematic analysis) should follow the trajectory of the matching point on the proximal phalanx surface due to natural finger motion, derived from the D-H model as described in Section 2.1. From now on, this trajectory will be denoted as *desired*. Evaluated referring to the MCP joint, this *desired trajectory* corresponds to a circumference arc since EE remains at the same distance from the MCP joint during hand opening and closing due to belonging to the same rigid body, the proximal phalanx. Specifically, the segment between the MCP joint and EE (O_3O_{EE}) represents the desired circumference radius. An in-depth kinematic study was conducted to ensure the end-effector correctly rotates around the MCP joint and covers the *desired trajectory* as much as possible.

The RCM mechanism has four bars: Link 1, Link 2, a third bar including Link 3 and the segment O_3O_{EE}, and another hand segment O_0O_3 as the mechanism frame. Besides, it has four revolute joints (three in the rigid architecture and one in hand, i.e., the MCP joint). According to the Grübler formula, the mechanism coupled with the hand has only 1 DoF. Thus, its kinematics can be solved as a function of a single independent variable represented in this study by the angle α_0, i.e., the angle that the segment O_3O_{EE} forms with the horizontal (see Fig. 2).

Kinematic analysis. The kinematic analysis allows for determining the pose of all the mechanism points. Fig. 2 shows how the reference systems were positioned. They are numerically labeled clockwise from the actuated joint ($O_0x_0y_0$, i.e., the joint that will be later coupled with the actuator) to the MCP joint ($O_3x_3y_3$). The joints centered in O_1 and O_2 are instead passive, and O_{EE} indicates the mechanism end-effector. As regards the coordinate systems, the $O_0x_0y_0$ frame is the fixed one, referring to which the kinematics is solved, while the others are integral to the corresponding numbered link; namely, $O_1x_1y_1$ is integral to Link 1, $O_2x_2y_2$ is integral to Link 2, and so on. The segment O_3O_{EE} forms the angle α_0 to the horizontal, and, as already said, it will be considered the kinematic study's only independent variable. Similarly, α_1, α_2, and α_{EE} are the angles Link 1 (of length a), Link 2 (of length b), and Link 3 (of length c) form to the horizontal. The segment O_3O_{EE} (d) is the radius of the circumference over which the end-effector shall move. Finally, the segment between O_0 and O_3 (e) is fixed and forms the angle ψ to the horizontal: both e and ψ depend on the target hand anatomy. The mechanism kinematics was solved based on the following conventions: (i) the symbol $\mathbf{O}_j^i$ indicates the jth joint position referred to the ith coordinates frame; (ii) similarly, $\mathbf{R}_j^i$ defines the jth frame orientation referred to the ith one (please note that, as the mechanism motion is planar, all rotation matrices express basic rotation about the z-axis); (iii) the superscript is omitted if the position is referred to the fixed frame $O_0x_0y_0$; (iv) goniometric operators as sine and cosine are replaced with s and c, respectively.

The joint poses are reported from Eq. (1) to Eq. (5):

$$\mathbf{O}_1 = -\mathbf{R}_1^0\mathbf{O}_0^1 \tag{1}$$

$$\mathbf{O}_2 = \mathbf{O}_1 + \mathbf{R}_1^0\mathbf{O}_2^1 \tag{2}$$

$$\mathbf{O}_{EE} = \mathbf{O}_2 + \mathbf{R}_2^0\mathbf{O}_{EE}^2 \tag{3}$$

$$\mathbf{O}_3 = -\mathbf{R}_3^0\mathbf{O}_0^3 \tag{4}$$

$$\mathbf{O}_{EE} = \mathbf{O}_3 + \mathbf{R}_3^0\mathbf{O}_{EE}^3 \tag{5}$$

It is worth noting that Eqs. (3) and (5) have the same results. Thus, only four vector equations describe the system state entirely, resulting in the following unknowns vector: $\mathbf{s} = [O_{1x}\ O_{1y}\ O_{2x}\ O_{2y}\ O_{EEx}\ O_{EEy}\ O_{3x}\ O_{3y}]' \in R^8$. Eqs. (1)–(5) depend on rotation matrices and position vectors. Into specifics, Eq. (1) can be expressed as follows:

$$\mathbf{O}_1 = -\begin{bmatrix} c_{\theta_1} & -s_{\theta_1} & 0 \\ s_{\theta_1} & c_{\theta_1} & 0 \\ 0 & 0 & 1 \end{bmatrix} \cdot \begin{bmatrix} -a \\ 0 \\ 0 \end{bmatrix} \tag{6}$$

Then, bearing in mind that vector $\mathbf{O}_2^1$ is defined as $\mathbf{O}_2^1 = -\mathbf{R}_2^1\mathbf{O}_1^2$, Eq. (2) is expressed as

$$\mathbf{O}_2 = -\begin{bmatrix} c_{\theta_1} & -s_{\theta_1} & 0 \\ s_{\theta_1} & c_{\theta_1} & 0 \\ 0 & 0 & 1 \end{bmatrix} \cdot \begin{bmatrix} -a \\ 0 \\ 0 \end{bmatrix} + - \begin{bmatrix} c_{\theta_1} & -s_{\theta_1} & 0 \\ s_{\theta_1} & c_{\theta_1} & 0 \\ 0 & 0 & 1 \end{bmatrix} \cdot \begin{bmatrix} c_{\theta_2} & -s_{\theta_2} & 0 \\ s_{\theta_2} & c_{\theta_2} & 0 \\ 0 & 0 & 1 \end{bmatrix} \cdot \begin{bmatrix} -b \\ 0 \\ 0 \end{bmatrix} \tag{7}$$

Once defined the pose $\mathbf{O}_{EE}^2$ as $\mathbf{O}_{EE}^2 = [cc_{\theta_{EE}}\ cs_{\theta_{EE}}\ 0]'$, Eq. (3) is made explicit as reported below:

$$\mathbf{O}_{EE} = -\begin{bmatrix} c_{\theta_1} & -s_{\theta_1} & 0 \\ s_{\theta_1} & c_{\theta_1} & 0 \\ 0 & 0 & 1 \end{bmatrix} \cdot \begin{bmatrix} -a \\ 0 \\ 0 \end{bmatrix} - \begin{bmatrix} c_{\theta_1} & -s_{\theta_1} & 0 \\ s_{\theta_1} & c_{\theta_1} & 0 \\ 0 & 0 & 1 \end{bmatrix} \cdot \begin{bmatrix} c_{\theta_2} & -s_{\theta_2} & 0 \\ s_{\theta_2} & c_{\theta_2} & 0 \\ 0 & 0 & 1 \end{bmatrix} \cdot \begin{bmatrix} -b \\ 0 \\ 0 \end{bmatrix} + \begin{bmatrix} c_{\theta_2} & -s_{\theta_2} & 0 \\ s_{\theta_2} & c_{\theta_2} & 0 \\ 0 & 0 & 1 \end{bmatrix} \cdot \begin{bmatrix} cc_{\theta_{EE}} \\ cs_{\theta_{EE}} \\ 0 \end{bmatrix} \tag{8}$$

Finally, Eq. (4) may be expressed as follows:

$$\mathbf{O}_3 = -\begin{bmatrix} 1 & 0 & 0 \\ 0 & 1 & 0 \\ 0 & 0 & 1 \end{bmatrix} \cdot \begin{bmatrix} -ec_\psi \\ -es_\psi \\ 0 \end{bmatrix} \tag{9}$$

$\mathbf{R}_3^0$ is an identity matrix since there is no relative rotation between $O_3x_3y_3$ and $O_0x_0y_0$ frames. The kinematic solution was verified by observing that Eqs. (3) and (5) define the same pose, considering that the vector $\mathbf{O}_{EE}^3$ can be expressed as $\mathbf{O}_{EE}^3 = [dc_{\alpha_0}\ ds_{\alpha_0}\ 0]'$.

It is fundamental to know how the angle α_0, indicative of the f/e movement, relates to the other joint angle, and each mechanism bar lengths to solve these equations as a function of it. Indeed, the unknowns vector $\mathbf{s} \in R^8$ can be expressed as a function of the angle α_0 and a vector $\mathbf{x} \in R^5$ of the bar dimensions, as follows: $s = f(\mathbf{x}, \alpha_0)$. In particular, vector $\mathbf{x}$ is defined as $\mathbf{x} = [a\ b\ c\ d\ e]'$. If such vector results from the optimization process described below, the relations between α_0 and the other joint angles were detected with the linkage *closure equation*. Referring to Fig. 2, it can be expressed as follows:

$$\boldsymbol{O_1O_0 + O_2O_1 + O_{EE}O_2 = O_3O_0 + O_{EE}O_3} \tag{10}$$

The following equations system results from the projection of Eq. (10) along the $O_0x_0y_0$-frame x and y axes, and bearing in mind that $\alpha_{EE} = \alpha_0 - \frac{\pi}{2}$:

$$\begin{cases} ac_1 + bc_2 + cs_0 = ec_\psi + dc_0 \\ as_1 + bs_2 - cc_0 = es_\psi + ds_0 \end{cases} \tag{11}$$

The system below is achieved by taking terms depending on α_2 to each equation left member:

$$\begin{cases} bc_2 = -ac_1 - cs_0 + ec_\psi + dc_0 \\ bs_2 = -as_1 + cc_0 + es_\psi + ds_0 \end{cases} \tag{12}$$

Eq. (13) below results from squaring and summing these two equations:

$$b^2 = a^2 + c^2 + d^2 + e^2 + 2ac(c_1s_0 - s_1c_0) + -2ae(c_1c_\psi + s_1s_\psi) - 2ad(c_1c_0 + s_1s_0) + -2ce(s_0c_\psi - c_0s_\psi) + 2ed(c_\psi c_0 + s_\psi s_0) \tag{13}$$

It is possible to solve it with the *added angle method* applied to an equation similar to $A = Bc_1 + Cs_1$. Thus, in Eq. (13), terms independent of α_1 may be collected on its left member, while those depending on c_{α_1} and s_{α_1} separately on the right. By doing so, coefficients A, B and C can be expressed as follows:

$$A = b^2 - a^2 - c^2 - d^2 - e^2 + 2ce(s_0c_\psi - c_0s_\psi) - 2ed(c_\psi c_0 + s_\psi s_0) \tag{14}$$

$$B = 2acs_0 - 2aec_\psi - 2adc_0 \tag{15}$$

$$C = -2acc_0 - 2aes_\psi - 2ads_0 \tag{16}$$

Thanks to the *added angle method* and goniometric function transformations, Eq. (13) can be expressed as

$$A = \sqrt{(B^2 + C^2)}\sin(\alpha_1 + \rho) \tag{17}$$

in which ρ is such that $\sin\rho = \frac{B}{\sqrt{B^2+C^2}}$ and $\cos\rho = \frac{C}{\sqrt{B^2+C^2}}$. Considering A, B and C only depending on α_0, once known vector $\mathbf{x}$, ρ is directly achievable by exploiting the *atan*2 function. Two alternative solutions result by reversing Eq. (17):

$$\alpha_{1,1} = \sin^{-1}\frac{A}{\sqrt{B^2 + C^2}} - \rho \tag{18}$$

$$\alpha_{1,2} = \pi - \sin^{-1}\frac{A}{\sqrt{B^2 + C^2}} - \rho \tag{19}$$

Among these, the solution with positive sine and cosine has to be chosen since, in this specific case study, it is enough that $\alpha_1 \in [0, \pi/2]$. These equations enable expressing α_1 as a function of α_0, while α_2 can be determined as a function of α_0 by reversing Eq. (12). Such considerations must be implemented in the MATLAB code to solve the kinematics. The values obtained for such angles due to the desired ROM show that α_1 decreases in this range, while α_2 and α_{EE} are negative and negatively increase. Instead, α_0 initially assumes positive and then negative values. Starting from the angles trend deduced from solving the *closure equation*, the relations between such angles and joint variables can be derived as reported below:

$$\theta_1 = \alpha_1 \tag{20}$$

$$\theta_2 = \alpha_2 - \alpha_1 \tag{21}$$

$$\theta_{EE} = \alpha_{EE} - \alpha_2 \tag{22}$$

$$\theta_0 = \alpha_0 - \psi \tag{23}$$

Eqs. (1)–(23) describe the kinematics of the coupled mechanism-finger system. In particular, they allow calculating the trajectory of $O_{EE}(\alpha_0)$ produced by the mechanism acting on the proximal phalanx; such a trajectory is henceforth referred to as the *actual trajectory*. Once identified both the *actual* and *desired trajectories*, they will be expressed in polar coordinates to facilitate the calculations. The kinematic synthesis of the rigid part aims to compare the two trajectories, thus optimizing the mechanism to minimize the error between them. In other terms, the final goal is to adapt the mechanism to the specific user's anatomy.

For this purpose, the study exploits a modified version of the *Nelder–Mead*-based optimization algorithm presented in [68]. This iterative procedure looks for the vector $\mathbf{x} \in S$ – where S is the so-called admissible region – that minimizes the objective function $f(\mathbf{x}) \in R$. Specifically, $\mathbf{S} \subset R^5$ is identified by all the constraints that characterize the mechanism in terms of dimensions, ROM, and geometry expressed as equations $\mathbf{h}(\mathbf{x}) = 0$ and inequalities $\mathbf{g}(\mathbf{x}) < 0$; the objective function $f(\mathbf{x})$ is, instead, defined as:

$$f(\mathbf{x}) = \alpha\Sigma\frac{\mathbf{e}_i(\theta_i)}{n} + (1 - \alpha)\max\mathbf{e}_i(\theta_i) \tag{24}$$

where $\mathbf{e}_i(\theta_i) = |\rho(\theta_i) - \rho^*(\theta_i)|$ represents the absolute value of the error between the actual, $\rho(\theta_i)$, and desired, $\rho^*(\theta_i)$, radial coordinates evaluated at the same ith angular coordinate θ_i, while $\alpha \in R$ is the weight to emphasize or not the contribution of the mean error versus the maximum error.

Starting from a first attempt vector $\mathbf{x}_0$, the first step of the actual optimization procedure consists of solving the mechanism kinematics to detect the O_{EE} *actual trajectory*; then, $f(\mathbf{x})$ is calculated, and its value memorized. A penalty is added to the objective function's final value if the current solution violates the constraints defining S. Then, for each iteration, a new vector $\tilde{\mathbf{x}}$ to solve the kinematics is produced, and the error between the compared trajectories is evaluated once again. The procedure is repeated for an arbitrary and finite number of times: the

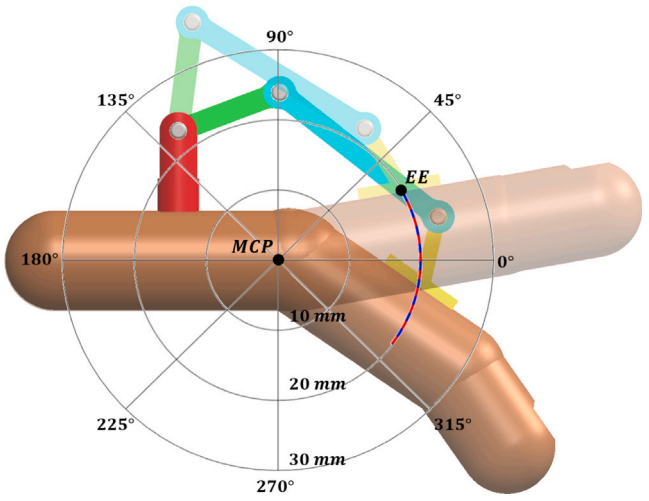

Fig. 3. The comparison between the *desired* and *actual trajectories* in polar coordinates, represented as continuous blue and dashed red lines, respectively.

vector $\mathbf{x}$ producing the lowest $f(\mathbf{x})$ is a local optimum that guarantees a minimum error between the compared trajectories and, possibly, satisfies all the problem constraints.

The following 12 constraint expressions, related to the mechanism geometry and overall dimensions, were introduced in the code to define the admissible region S:

$$\begin{array}{cc} O_{1x,min} > 0 & O_{3x} > 0 \\ O_{1y,min} > 0 & O_{3x} < 40 \\ O_{1y,max} < 20 & b > 0 \\ O_{2x,(1)} < O_{EEx,(1)} & c > 0 \\ O_{1x,(1)} < O_{2x,(1)} & \alpha_{1max} < 85° \\ O_{3x} < O_{EEx} & \alpha_{1min} > 0° \end{array} \tag{25}$$

where the exploitation of the subscript (1) indicates that the variable is evaluated at the first ROM step, corresponding to the finger maximum extension (or complete opening).

The inputs to the code are only the first attempt vector, the hand palm and finger thickness, and the vertical distance between the hand back and actuated joint. By doing so, the actuated joint position, thus that of the transmission system on the hand back, is derived from the optimization result. The resulting vector $\mathbf{x}$, including the dimensions for designing the mechanism bars in the CAD software SolidWorks through a parametric CAD model, is exploited to solve the four-bar mechanism kinematics and derive the EE actual trajectory, shown in red in Fig. 3, where it is compared with the desired one, blue colored. It is important to point out that in such a case, the maximum error evaluated during different optimization processes is on the order of 10^{-6}. This is probably due to the straightforward *desired trajectory*, which allows easily detecting a mechanism whose end-effector covers an *actual trajectory* similar to the desired one.

Kinetostatic analysis. A 15-N force perpendicular to the proximal phalanx (see Fig. 4) was targeted to achieve *efficacy-in-ALDs* requirement [63]. Thanks to the possibility of neglecting dynamic effects – due to the low masses and velocities involved – the mechanism kinetostatic analysis was performed to calculate the torque τ_z to be applied to the mechanism actuated joint (O_0) so that its end-effector (O_{EE}) exerts such a desired force. This particular data will then be necessary when choosing the components of the actuation system and dimensioning the parts. The analysis was conducted by exploiting the *Principle of Virtual Works*. In the case study, the only external forces applied to the mechanism are the torque $\tau_z \in R$ and force $\mathbf{F} \in R^3$, arranged in the load configuration shown in Fig. 4. Considering α_0 as the generalized coordinate, the *Principle of Virtual Works* can be formalized as follows:

$$\tau_z \ \delta\alpha_1(\alpha_0) + \mathbf{F}^T \cdot \delta\mathbf{O_{EE}}(\alpha_0) = 0 \tag{26}$$

where $\delta\alpha_1 \in R$ and $\delta\mathbf{O_{EE}} \in R^3$ are the virtual displacement of the actuated joint and the EE, respectively. Both $\delta\alpha_1$ and $\delta\mathbf{O_{EE}}$ can be expressed as a function of the generalized coordinate as reported below:

$$\delta\alpha_1(\alpha_0) = \frac{\partial\alpha_1}{\partial\alpha_0}\delta\alpha_0 \tag{27}$$

$$\delta\mathbf{O_{EE}}(\alpha_0) = \frac{\partial\mathbf{O_{EE}}}{\partial\alpha_0}\delta\alpha_0 = \begin{bmatrix} \frac{\partial O_{EEx}}{\partial\alpha_0} \\ \frac{\partial O_{EEy}}{\partial\alpha_0} \\ 0 \end{bmatrix}\delta\alpha_0 \tag{28}$$

Finally, considering $\mathbf{F}^T = [F_x \ F_y \ 0]$, Eq. (26) can be rewritten as:

$$\tau_z \frac{\partial\alpha_1}{\partial\alpha_0}\delta\alpha_0 + [F_x \ F_y \ 0] \cdot \begin{bmatrix} \frac{\partial O_{EEx}}{\partial\alpha_0} \\ \frac{\partial O_{EEy}}{\partial\alpha_0} \\ 0 \end{bmatrix}\delta\alpha_0 = 0 \tag{29}$$

where $\frac{\partial\alpha_1}{\partial\alpha_0}$ can be deduced from Eq. (18) as follows:

$$\frac{\partial\alpha_1}{\partial\alpha_0} = \frac{\partial(\sin^{-1}\frac{A}{\sqrt{B^2+C^2}} - \rho)}{\partial\alpha_0} \tag{30}$$

and $\frac{\partial\mathbf{O_{EE}}}{\partial\alpha_0}$ is derived from Eq. (5), resulting in the vector $[-ds_0 \ dc_0 \ 0]'$.

Eq. (29) was implemented in MATLAB and the kinetostatic analysis was solved by varying the generalized coordinate α_0 within the ROM $[-37° \ 32°]$, which resulted from solving the hand kinematic model. The resulting τ_z trend is reported in Fig. 4, and showed a maximum of 245.47 Nmm when the mechanism is fully closed ($\alpha_0 = -37°$).

2.3.2. The soft architecture

The soft architecture is designed to enable the f/e movement of the thumb distal phalanx (and the intermediate one for the other fingers) while keeping the overall mechanism dimensions above the finger as reduced as possible. Cable-driven gloves [35,36,38,40], fiber-reinforced [21], polymer-or-elastomer-based [33], and fabric-based [34] solutions are the most frequently employed in the literature. However, as mentioned in Section 2.2, they usually require remote location of some components (e.g., electronic components, actuators, power supply) to achieve a better distribution of masses, thus reducing the device wearability and end-user mobility. In addition, they prevent the sense of touch. Therefore, layered-spring systems, already exploited in [39], were chosen for this purpose. However, if in [39] they are driven by a rack-and-pinion system actuated by DC motors through Bowden cables, in the study presented in this paper, two flat springs determine the f/e movement only thanks to the relative motion between Link 2 and 3 (see Fig. 5). The spring closest to the finger (red colored in figure), which is at a distance h_c to the proximal-phalanx axis, is fixed to the proximal-phalanx end-effector and can slide into the distal-phalanx one. The furthest spring (gray colored) is placed at a distance of h_f from the distal-phalanx axis. Its ends are fixed to Link 2 and the distal-phalanx end-effector, while the spring itself may slide into the proximal-phalanx end-effector. If the spring closest to the finger has the sole scope of adding stability to the system, the furthest one determines the distal phalanx f/e only due to the relative motion between Link 2 and 3. Specifically, when the rigid architecture actuates the proximal phalanx f/e, its end-effector rotates around O_2 (see Fig. 2) according to the four-bar kinematics, and the relative movement between Link 2 and 3 determines the variation of the distance separating point B and A (see Fig. 5). Referring to Fig. 5, it is worth noting, indeed, that the angle γ decreases during the flexion movement that produces an approach of point B to point A. Since the flat spring is inelastic in the longitudinal direction and not fixed to Link 3, this movement causes the spring

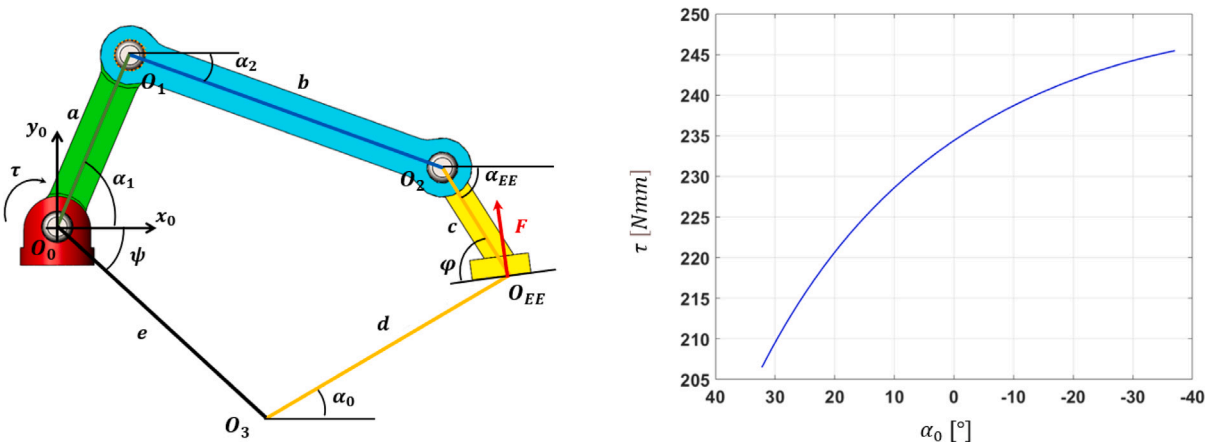

Fig. 4. On the left, the schematic mechanism representation with external forces applied, and, on the right, the torque trend as a function of α_0, resulting from the kinetostatic analysis.

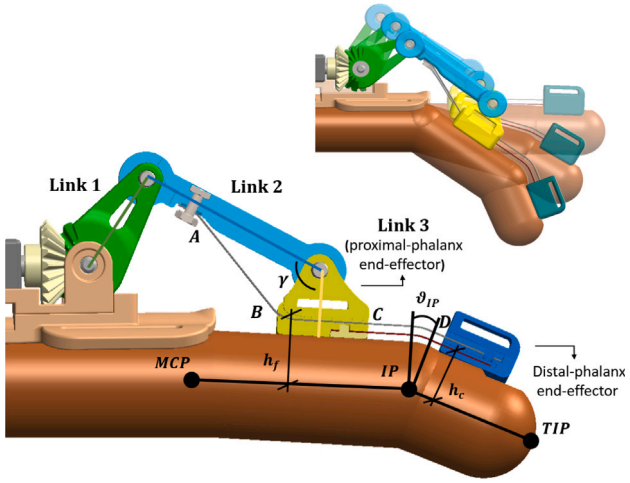

Fig. 5. Sectional view of the soft architecture [73]. A indicates the housing for the spring end to Link 2, B is the inlet for the spring into the proximal-phalanx end-effector, C the exit point of the furthest spring from the proximal-phalanx end-effector, while D shows the spring inlet to the distal-phalanx end-effector. On the top, the flexion movement.

to slide into the housing, which has been designed in the proximal-phalanx end-effector for this purpose. For a first approximation, the spring sliding into Link 3 can be compared to the modification of the AB distance during the flexion movement. In addition, the reduction of the AB distance can be translated into the increase of the CD distance, measured along the spring, and not as minimum distance among these points. Geometric considerations show that the springs are compelled to flex around the IP joint, which represents a RCM for this architecture, thus producing the distal-phalanx flexion by pushing its end-effector to which the spring is fixed. On the contrary, the spring produces the distal-phalanx extension when the four-bar mechanism causes the proximal-phalanx extension. This condition, indeed, determines the increase of the AB distance due to reverse sliding. Accordingly, the CD distance reduces, and the distal-phalanx end-effector is pulled.

The correlation between the sliding l of the furthest spring into the proximal-phalanx end-effector and IP joint f/e angle θ_{IP} results as follows:

$$l = \frac{2\pi h_f}{360}\theta_{IP} \ . \tag{31}$$

It is worth noting that the soft architecture is not involved in the optimization procedure described above, but the springs' length can

Table 3
The four-bar mechanism dimensions resulted from the optimization process after the mentioned modifications.

a [mm]	b [mm]	c [mm]	d [mm]	e [mm]
26.26	27.21	19.95	18.04	27.55

be evaluated considering the phalanges lengths, EE dimensions, and optimized dimensions of the rigid architecture. Specifically, the springs' configuration (Fig. 5) is determined by the point A position, h_f (thus the point B position), and h_c. All these parameters affect the achievable IP joint f/e range, evaluable through Eq. (31). For each tested configuration, the maximum sliding l was evaluated as the variation of the distance AB among the rest ($\theta_{MCP} = 0°$) and the complete finger flexion ($\theta_{MCP} = -90°$) condition. The corresponding θ_{IP} was calculated by reversing Eq. (31), and the configuration enabling the more extensive IP joint range – $\simeq 60°$ in flexion and $\simeq 10°$ in extension – was chosen. Even if the complete IP ROM ($\simeq 110°$) is not reachable, such a configuration can be considered acceptable according to [74]. At the moment, the hybrid architecture, including the soft part, is under study. Specifically, its multibody model is being simulated. First results are showing that a single flat spring 0.2 mm thick and 6 mm wide enables to cover the evaluated reachable ROM ($\simeq 70°$ of which $\simeq 10°$ in extension and $\simeq 60°$ in flexion). However, more precise conclusion can be drawn after further investigation.

2.4. Mechanism embodiment

This section will briefly discuss the embodiment of the mechanism synthesized in the previous section. After some iterations, in which different module components arrangement were tried to reduce the overall dimensions above the MCP joint to exploit the same module for all the fingers, and its mobility was tested, a definitive thumb module prototype was conceived and developed. Its CAD model and an exploded view showing its main components are reported in Fig. 6. Referring to Fig. 2, the actuated joint (O_0) was relocated above the MCP joint (O_3). The optimization process was repeated with the modified kinematics, and the resulting vector $\mathbf{x}$ is reported in Table 3. Thanks to this modification, it was possible to add a passive a/a DoF to the actuated joint, which is realized by introducing a cylindrical pin transversely to the driven shaft and Link 1 (see Figs. 6 and 7). By doing so, the mechanism can reach a maximum of 18° of abduction and 10° of adduction, as reported in Fig. 7. According to the Von Mises calculations, a 2-mm diameter and 8-mm length cylindrical AISI 303 pin resulted sufficient to withstand the involved stresses.

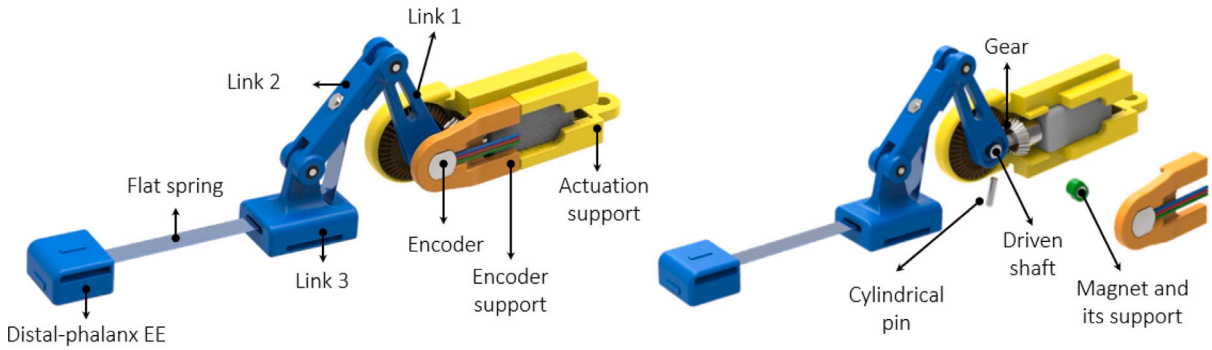

Fig. 6. The thumb module prototype: on the left, the whole module, and on the right, an exploded view of the magnet and its housing (green colored), the driven shaft, integral to Link 1, and the cylindrical pin for the a/a movement.

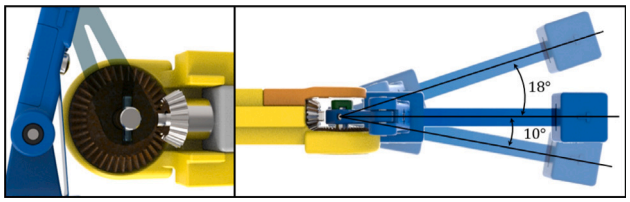

Fig. 7. The a/a movement: a view on the cylindrical, on the left, and the achieved a/a ROM, on the right.

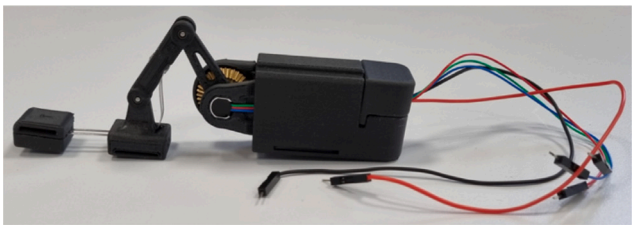

Fig. 8. The prototype of the hybrid finger mechanism, embodiment of the design process.

Table 4
The transmission gears features.

	Driven wheel	Driving wheel
Module	0.5	0.5
Material	Brass	C45
N° of Teeth	40	20
Reference diameter [mm]	20	10
Inner diameter [mm]	4	3
Tip diameter [mm]	20.45	10.89
Width [mm]	3.2	3.2
Face angle	66°	29° 8’

Taking into account the target torque (238.86 Nmm) evaluated as in Section 2.3.1 for the new version of the finger-handling mechanism, a Pololu Micro Metal Gearmotor 380:1 Low-Power (LP 6V) was chosen for this specific application. It weighs 10 g, and its overall dimensions are $26\times12\times10$ mm^3, enabling exploiting analogous actuators for all the other fingers. Its peak power is 0.27 W around the operating conditions, and a no-load speed of 36 rpm characterizes it. At stall condition, it delivers a torque of 29 kgmm (284.49 Nmm) draining 0.35 A, which is high enough to exert the target torque and prevent overheating issues. The operating range velocity was considered suitable to exploit a 1:2 gear ratio, avoiding bulky transmission systems. A coupling of steel (C45) and brass bevel gears (gear ratio = 1:2) from KG Gears was exploited for the driving and driven wheels, respectively. Table 4 summarizes their main features. According to calculations for tooth bending stress, they are verified to withstand the maximum transmissible torque due to the transmission gear ratio, achieving 58 kgmm (568.98 Nmm). The thumb-handling mechanism components are designed to be 3D printed in ABS CF10, for its remarkable mechanical characteristics, and on the basis of the results of static FEM analyses performed at the complete finger closure configuration, i.e., the worst loading condition according to calculation in Section 2.3.1. The driven shaft was designed according to the stresses due to the gears exploited and mechanism. Only one flat spring in spring steel with a section area of 0.2×6 mm^2 has been exploited for this prototype to enable to target ROM coverage. It has two drilled holes at its ends to fix it to Link 2 and the distal-phalanx end-effector through little screws (M2).

Finally, a linear-voltage non-contact rotary encoder from RLS (RM08VB0010B02L2G00 - RMM3010A1A00) was added (as shown in Fig. 6) to provide a direct measure of the finger f/e angle. Fig. 8 shows the final prototype presented in this section.

3. Tests and results

The resulting actuation module, including its external housing, is 23 mm wide, and 28 mm high, and 72.5 mm long. The mechanism reaches a maximum height to the hand back of about 38 mm. Considering that such a module is designed to be repeated for all the fingers, the HES weight on the hand back was estimated to reach about 300 g, including the case that shall house the finger modules. This prototype cost about 240 €, including the 3D printed and commercial components. Thus, it can be estimated that the total cost of the whole prototype, also considering the electronic components for power supply and control, is around 1500 €. The results of the preliminary tests undergone by the manufactured prototype will be reported in this section. Upon signing an informed consent form, a healthy subject was involved. The specific user anatomic parameters were collected, and used to optimize and customize the prototype.

3.1. ROM evaluation

The first crucial step is understanding if the hybrid architecture effectively followed the finger f/e movement while covering the user’s finger ROM as much as possible. To this aim, some motion tests were performed after decoupling the mechanism from the actuation system and wearing it by the subject. The subject was then asked to flex and extend the thumb finger ten times – preventing metacarpal movement as much as possible – while being filmed. The same task was performed with and without the finger mechanism worn (see Fig. 9). The videos were elaborated using the open software Kinovea. Maximum f/e angles of the MCP (θ_{MCP}) and IP (θ_{IP}) joints were measured, and mean and standard deviation values are reported in Table 5. The evaluation highlighted an almost complete coverage of the MCP joint ROM while,

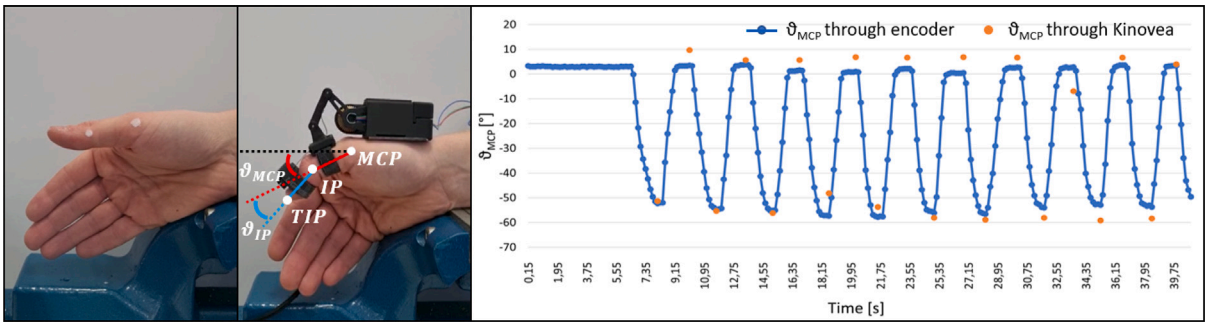

Fig. 9. On the left, the setup for the ROM measurements during the thumb f/e while the subject wears and does not wear the prototype. On the right, the θ_{MCP} angles evaluated by giving encoder data as input to the kinematic function (blue line) compared with the maximum f/e angles extracted from the recorded videos through Kinovea (orange points).

Table 5
The mean value and standard deviation of the MCP and IP joints angles (θ_{MCP} and θ_{IP}, respectively) while the subject wears (*Worn device)* and does not wear the device (*Unworn device)*.

		Unworn device	Worn device
Extension	θ_{MCP} [°]	3.53 ± 1.94°	4.26 ± 3.1°
	θ_{IP} [°]	17.21 ± 2.49°	9.64 ± 2.72°
Flexion	θ_{MCP} [°]	−54.69 ± 1.5°	−55.74 ± 3.48°
	θ_{IP} [°]	−60.25 ± 3.65°	−55.26° ± 2.38°

globally, the mechanism allows for the coverage of 84% of the IP joint ROM.

A subsequent investigation exploited the encoder to verify and validate the θ_{MCP} angle measurements taken through Kinovea. Indeed α_1 (the angle the Link 1 forms to the horizontal, shown in Fig. 2) can be measured directly by the newly added encoder. An Arduino Nano Every was exploited for this task. From the kinematic study reported in Section 2.3.1, angle α_0, thus also θ_{MCP}, can be expressed and evaluated as a function of α_1. The calculations were performed in MATLAB, and the comparison between the θ_{MCP} values resulting from the two acquisition methods is reported in Fig. 9. It is interesting to observe the comparable measurements in correspondence with the maximum f/e conditions.

From the kinematic test, it has been possible to determine the relation between each joint angular coordinate and the angle α_1. The scene was filmed while the subject performed five finger openings and closings. Still exploiting Kinovea, the angles θ_{MCP}, θ_{IP}, and α_1 were measured each 0.15 s to detect the trend of the finger joints angular coordinates in relation to that depending on the motor input. α_1, indeed, varies from the motor angle by a constant corresponding to the transmission ratio chosen (1:2). Such measurements are reported as blue (θ_{MCP}) and orange (θ_{IP}) dots in Fig. 10. A linear regression resulted enough to approximate the relation between the angular coordinates θ_{MCP} and α_1 ($R^2 = 0.9959$), while a second-order polynomial best relates θ_{IP} and α_1 ($R^2 = 0.98$).

3.2. Forces evaluation

In addition to ROM evaluation, measurements of the exerted forces were performed. A force sensing resistor (FSR 406, coupled with a 3.3 kΩ resistor) and dual motor drivers (TB6612FNG) by Pololu were hooked up to the same Arduino Nano Every to control the module actuator and collect indirect measures of the forces the actuated finger can exert on objects. Characterizing the FSR is mandatory to derive the force applied based on the recorded output voltage. A custom 3D-printed housing for the FSR, shown on the top of Fig. 11, was designed. It consists of three parts: (i) the main body to house the sensor; (ii) the coverage to be used only during the force measurement phase; (iii) an intermediate part designed to determine a flat and stable surface for placing masses during the sensor characterization

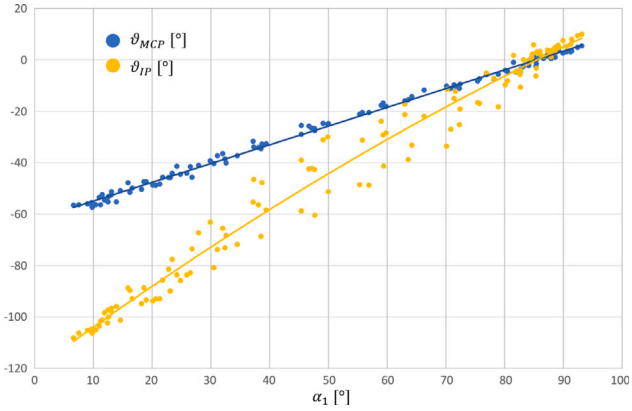

Fig. 10. The relation between θ_{MCP} and α_1, blue colored, and that between θ_{IP} and α_1, orange colored, resulted from the kinematic test.

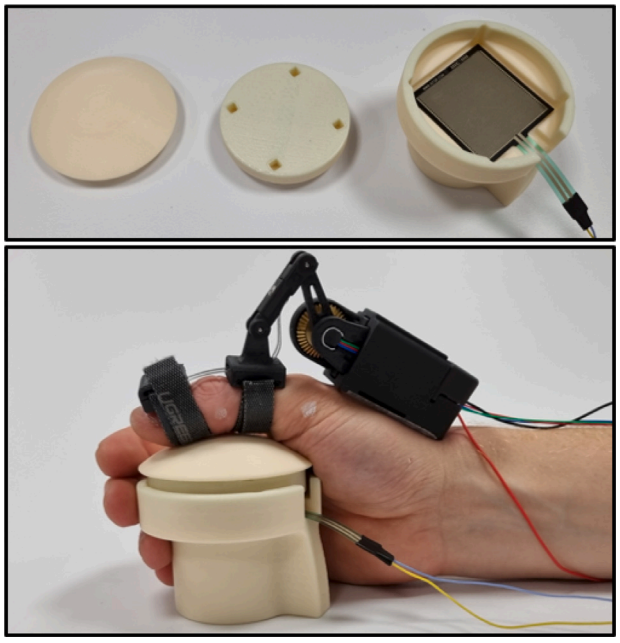

Fig. 11. The component designed for housing the FSR during its characterization and force measurement, on the top. From the left to the right, the three parts composing it are shown: (i) the coverage, (ii) the intermediate part, and (iii) the main body. On the bottom, instead, the configuration in which the measurements are taken is shown.

while distributing the load evenly on the sensor surface. Continuous incremental loading and unloading cycles (i.e., the masses were added

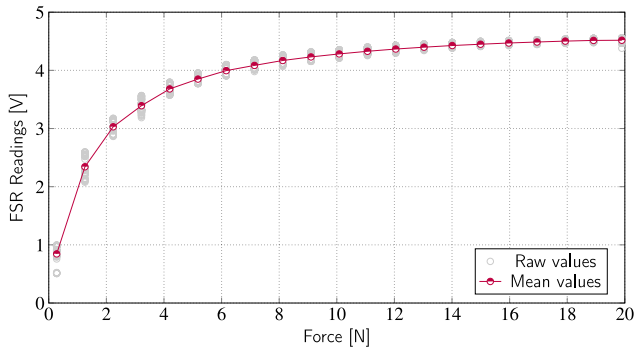

Fig. 12. FSR characterization: the graph shows the FSR voltage readings as the force applied to the sensor changes. The measurements (raw values) taken during the three repetitions are gray-colored, while the mean values are purple-highlighted.

Table 6
The mean output force values for seven f/e movements.

	M1	M2	M3	M4	M5	M6	M7
Force [N]	5,94	7,81	16,78	11,31	12,79	11,66	7,89

or removed by incremental steps without completely unloading the sensor between different measures) were performed according to the following setup. Measures were acquired at 1 Hz. Every 20 s, a 100-g load was added: the sensor was given ten seconds to stabilize; then, the remaining ten measures were considered for the characterization. The complete loading/unloading cycle (from 0 to 2000 g and vice versa) was performed three times. The recorded outputs (i.e., the 10-bit conversion operated by the microcontroller ADC) during the three cycles are reported in Fig. 12. For each interval, the mean value was calculated. The mean values were then linearly interpolated two by two to use that curve to derive the mass (i.e., the force) corresponding to the measured output during the tests. The interpolating curve is shown in Fig. 12.

When the sensor characterization was completed, the subject was asked to wear the device for the actual force measurements. The subject was also asked to remain as passive as possible while the actuation system drove the mechanism. The experimenter sent extension, flexion, and resting commands to the finger module via serial communication. The experimental setup, as visible on the bootom of Fig. 11, involved the thumb being pressed by the mechanism against the FSR sensor housing. The actuator power supply was limited to up to 90% of the stall current to avoid excessive overheating. As chosen during the characterization, the second ten recorded measures were considered after the subject's finger got in touch with the sensor. Several repetitions were performed. However, only seven have tuned out to be appropriately acquired. The average of the ten acquisitions was calculated for each repetition; then, the corresponding force was extrapolated through the sensor characterization. Table 6 summarizes the results of this test. It is worth mentioning that the thumb module was designed to exert about 15 N on the finger and withstand the actuator stall condition. The measurements proposed in this subsection show that the target force was rather achieved by calculating a mean value of about 10.6 N and observing a maximum value that reaches 16.78 N. The significant variability in the results can be attributed in the first instance to the involvement of the human subject in the experimental setup.

4. Discussion

The finger mechanism described in this paper represents a valuable starting point for developing an assistive hand exoskeleton, which meets the requirements listed in Section 2.2 and stands out within the state of the art. Thanks to its *lightness and small size*, the same module can be implemented for all the fingers, thus enabling *independent finger motion*. The whole device estimated weight, although very close to the threshold on the hand, is comparable to or less than the ones listed in Table 2 except for a few. Indeed, [20,35,53] present lighter devices, but only some fingers are actuated; in [22], most components are remotely placed, leaving only cables on the finger, compromising the system wearability. Similarly, in [34], the pneumatic actuators of the soft fabric glove are displaced from the hand, while the device presented in [37] exploits only two motors to move all the fingers, and no information about the electronic components and power supply system location is reported.

Finally, the force measurements reported in Section 3.2 show that the device can be truly *effective in ADLs*, bearing in mind the force benchmarking reported in [63]. To the authors' knowledge, no other devices show the potential of exerting such forces while remaining completely wearable. At the moment, Velcro straps connect the device to the hand, *preserving the sense of touch*. Its estimated cost makes it *affordable*, even if no easy terms of comparison are available. Finally, exploiting a RCM mechanism and a validated kinematic optimization procedure to tailor the device to the user's anatomy ensure the *safety* and promote *comfort*. It is worth noting that the actuator has a minimum back-drivability that add safety strength to the new finger module since in case of an operating failure, the mechanism can be manually returned to the resting condition.

5. Conclusions

This manuscript presents the synthesis and design of a finger exoskeleton module for its f/e movement. The design choices underlying this module are based on the desire to develop a fully wearable and portable hand exoskeleton for assistance during daily life. After exposing the main requirements for these devices, the design choices for pursuing them were discussed based on the current solutions available in the literature. An original hybrid architecture (including rigid and soft elements) was presented and analyzed. Detailed kinematic and kinetostatic analyses enabled designing a mechanism fully optimized on the anatomy of the specific user, and capable of covering most of the finger ROM and exerting high enough forces to be effective during ADLs. Thus, unlike other solutions in the literature, this mechanism combines the effectiveness in force transmission typical of rigid architectures with the lightness, compliance, and reduced bulk of soft solutions. The embodiment of the theoretical analysis into an actual prototype allowed for validating the design procedure.

Indeed, the manufactured prototype resulted sufficiently small to be replicated for all the other fingers and still keep the system all on the hand; the new design allows for the finger a/a movement. Besides, the exerted forces were measured by using an FSR. The results showed a remarkable ROM coverage (with a minimum of 84%) and auspicious performance in force exertion (up to 16.78 N per finger). Expanding the observation to the whole hand exoskeleton that can be developed based on the finger module described in this paper, wearability, portability, independent finger motion, and affordability may be achieved.

Future developments will regard improvements to the soft architecture to increase the ROM coverage, the module redesign to enclose the gears and add mechanical stops, thus avoiding dirt infiltration and increasing safety, and the whole device design. Besides, the control system, including the definition of the high-level control strategy and all the electronic components necessary for the proper device operation, is currently being analyzed. All such developments, planned within an ongoing three-year research project, will lead the device Technology Readiness Level transition from 4 to 6. Finally, tests will be performed on healthy subjects and patients to verify the actual usability of the resulting HES. It can be noted that possible patients are all those who have residual muscular activity due to exploiting surface electromyography as an intention detection method. First tests are scheduled with post-stroke patients, at the suggestion of and in collaboration with clinical professionals, project partners. Also, the exploitation of such a device in a rehabilitation program is now under feasibility analysis.

Declaration of competing interest

The authors declare that they have no known competing financial interests or personal relationships that could have appeared to influence the work reported in this paper.

Data availability

Data will be made available on request.

Acknowledgments

The authors acknowledge the support of the European Union by the Next Generation EU project ECS00000017 'Ecosistema dell'Innovazione' Tuscany Health Ecosystem (THE, PNRR, Spoke 4: Spoke 9: Robotics and Automation for Health) and of the Fondazione CR Firenze by the R3COVER project.

References

[1] Cieza A, Causey K, Kamenov K, Hanson SW, Chatterji S, Vos T. Global estimates of the need for rehabilitation based on the global burden of disease study 2019: A systematic analysis for the global burden of disease study 2019. Lancet 2020;396(10267):2006–17.
[2] Carmeli E, Patish H, Coleman R. The aging hand. J Gerontol Ser A: Biol Sci Med Sci 2003;58(2):M146–52.
[3] İncel NA. Functional assessment in geriatric hand. In: Hand function. Springer; 2019, p. 211–25.
[4] den Hollander M, Hoekstra A. Hand function in children with congenital disorders. In: Hand function. Springer; 2019, p. 189–200.
[5] Duncan SF, Saracevic CE, Kakinoki R. Biomechanics of the hand. Hand Clinics 2013;29(4):483–92.
[6] Regal S, Maschke S, Li Z-M. Hand and wrist biomechanics. In: Frontiers in orthopaedic biomechanics. Springer; 2020, p. 89–104.
[7] Duruöz MT. Assessment of hand functions. In: Hand function. Springer; 2014, p. 41–51.
[8] du Plessis T, Djouani K, Oosthuizen C. A review of active hand exoskeletons for rehabilitation and assistance. Robotics 2021;10(1):40.
[9] Yue Z, Zhang X, Wang J. Hand rehabilitation robotics on poststroke motor recovery. Behav Neurol 2017.
[10] Zhang K, Chen X, Liu F, Tang H, Wang J, Wen W. System framework of robotics in upper limb rehabilitation on poststroke motor recovery. Behav Neurol 2018;2018.
[11] Duret C, Grosmaire A-G, Krebs HI. Robot-assisted therapy in upper extremity hemiparesis: Overview of an evidence-based approach. Front Neurol 2019;10:412.
[12] Aggogeri F, Mikolajczyk T, O'Kane J. Robotics for rehabilitation of hand movement in stroke survivors. Adv Mech Eng 2019;11(4):1687814019841921.
[13] Huang X, Naghdy F, Naghdy G, Du H, Todd C. Robot-assisted post-stroke motion rehabilitation in upper extremities: a survey. Int J Disabil Hum Dev 2017;16(3):233–47.
[14] Chen B, Zi B, Wang Z, Qin L, Liao W-H. Knee exoskeletons for gait rehabilitation and human performance augmentation: A state-of-the-art. Mech Mach Theory 2019;134:499–511.
[15] Sanjuan J, Castillo AD, Padilla MA, Quintero MC, Gutierrez E, Sampayo IP, et al. Cable driven exoskeleton for upper-limb rehabilitation: A design review. Robot Auton Syst 2020;126:103445.
[16] Li J, Zheng R, Zhang Y, Yao J. IHandRehab: An interactive hand exoskeleton for active and passive rehabilitation. In: 2011 IEEE international conference on rehabilitation robotics. IEEE; 2011, p. 1–6.
[17] Maciejasz P, Eschweiler J, Gerlach-Hahn K, Jansen-Troy A, Leonhardt S. A survey on robotic devices for upper limb rehabilitation. J Neuroeng Rehabil 2014;11(1):1–29.
[18] Diez JA, Blanco A, Catalán JM, Badesa FJ, Lledó LD, Garcia-Aracil N. Hand exoskeleton for rehabilitation therapies with integrated optical force sensor. Adv Mech Eng 2018;10(2):1687814017753881.
[19] Bartalucci L, Secciani N, Gelli J, Valle AD, Ridolfi A, Allotta B. Rehabilitative hand exoskeleton system: a new modular mechanical design for a remote actuated device. In: The international conference of IFToMM ITALY. Springer; 2020, p. 128–36.
[20] Lambercy O, Schröder D, Zwicker S, Gassert R. Design of a thumb exoskeleton for hand rehabilitation. In: Proceedings of the 7th international convention on rehabilitation engineering and assistive technology. Singapore Therapeutic, Assistive & Rehabilitative Technologies (START) Centre; 2013, p. 41.
[21] Polygerinos P, Wang Z, Galloway KC, Wood RJ, Walsh CJ. Soft robotic glove for combined assistance and at-home rehabilitation. Robot Auton Syst 2015;73:135–43.
[22] Randazzo L, Iturrate I, Perdikis S, Millán JdR. Mano: A wearable hand exoskeleton for activities of daily living and neurorehabilitation. IEEE Robot Autom Lett 2017;3(1):500–7.
[23] Wang D, Meng Q, Meng Q, Li X, Yu H. Design and development of a portable exoskeleton for hand rehabilitation. IEEE Trans Neural Syst Rehabil Eng 2018;26(12):2376–86.
[24] Bouteraa Y, Abdallah IB, Elmogy AM. Training of hand rehabilitation using low cost exoskeleton and vision-based game interface. J Intell Robot Syst 2019;96(1):31–47.
[25] Zhang F, Lin L, Yang L, Fu Y. Design of an active and passive control system of hand exoskeleton for rehabilitation. Appl Sci 2019;9(11):2291.
[26] Sandison M, Phan K, Casas R, Nguyen L, Lum M, Pergami-Peries M, et al. Handmate: Wearable robotic hand exoskeleton and integrated android app for at home stroke rehabilitation. In: 2020 42nd annual international conference of the IEEE engineering in medicine & biology society. IEEE; 2020, p. 4867–72.
[27] Topini A, Sansom W, Secciani N, Bartalucci L, Ridolfi A, Allotta B. Variable admittance control of a hand exoskeleton for virtual reality-based rehabilitation tasks. Front Neurorobot 2021;188.
[28] Lambercy O, Ranzani R, Gassert R. Robot-assisted rehabilitation of hand function. In: Rehabil robot. Elsevier; 2018, p. 205–25.
[29] Rodgers H, Bosomworth H, Krebs HI, van Wijck F, Howel D, Wilson N, et al. Robot assisted training for the upper limb after stroke (RATULS): A multicentre randomised controlled trial. Lancet 2019;394(10192):51–62.
[30] Ho N, Tong K, Hu X, Fung K, Wei X, Rong W, et al. An EMG-driven exoskeleton hand robotic training device on chronic stroke subjects: Task training system for stroke rehabilitation. In: 2011 IEEE international conference on rehabilitation robotics. IEEE; 2011, p. 1–5.
[31] Tong K, Ho S, Pang P, Hu X, Tam W, Fung K, et al. An intention driven hand functions task training robotic system. In: 2010 Annual international conference of the IEEE engineering in medicine and biology. IEEE; 2010, p. 3406–9.
[32] Yun Y, Dancausse S, Esmatloo P, Serrato A, Merring CA, Agarwal P, et al. Maestro: An EMG-driven assistive hand exoskeleton for spinal cord injury patients. In: 2017 IEEE international conference on robotics and automation. IEEE; 2017, p. 2904–10.
[33] Ang BW, Yeow C-H. Print-it-yourself (PIY) glove: a fully 3D printed soft robotic hand rehabilitative and assistive exoskeleton for stroke patients. In: 2017 IEEE/RSJ international conference on intelligent robots and systems. IEEE; 2017, p. 1219–23.
[34] Cappello L, Meyer JT, Galloway KC, Peisner JD, Granberry R, Wagner DA, et al. Assisting hand function after spinal cord injury with a fabric-based soft robotic glove. J Neuroeng Rehabil 2018;15(1):1–10.
[35] In H, Kang BB, Sin M, Cho K-J. Exo-glove: A wearable robot for the hand with a soft tendon routing system. IEEE Robot Autom Mag 2015;22(1):97–105.
[36] Rose CG, O'Malley MK. Hybrid rigid-soft hand exoskeleton to assist functional dexterity. IEEE Robot Autom Lett 2018;4(1):73–80.
[37] Zhao L, Xie C, Song R. Design and validation of a wearable hand exoskeleton system. In: 2020 5th International conference on advanced robotics and mechatronics. IEEE; 2020, p. 559–63.
[38] Yurkewich A, Kozak IJ, Ivanovic A, Rossos D, Wang RH, Hebert D, et al. Myoelectric untethered robotic glove enhances hand function and performance on daily living tasks after stroke. J Rehabil Assist Technol Eng 2020;7:2055668320964050.
[39] Dittli J, Hofmann U, Bützer T, Lambercy O, Gassert R. Remote actuation systems for fully wearable assistive devices: Requirements, selection, and optimization for out-of-the-lab application of a hand exoskeleton. Front Robot AI 2020;7:187.
[40] Popov D, Gaponov I, Ryu J-H. Portable exoskeleton glove with soft structure for hand assistance in activities of daily living. IEEE/ASME Trans Mechatronics 2016;22(2):865–75.
[41] Secciani N, Pagliai M, Buonamici F, Vannetti F, Volpe Y, Ridolfi A. A novel architecture for a fully wearable assistive hand exoskeleton system. In: The international conference of IFToMM ITALY. Springer; 2020, p. 120–7.
[42] Secciani N, Brogi C, Pagliai M, Buonamici F, Gerli F, Vannetti F, et al. Wearable robots: An original mechatronic design of a hand exoskeleton for assistive and rehabilitative purposes. Front Neurorobot 2021;15.
[43] Esposito D, Centracchio J, Andreozzi E, Savino S, Gargiulo GD, Naik GR, et al. Design of a 3D-printed hand exoskeleton based on force-myography control for assistance and rehabilitation. Machines 2022;10(1):57.
[44] Heo P, Gu GM, Lee S-j, Rhee K, Kim J. Current hand exoskeleton technologies for rehabilitation and assistive engineering. Int J Precis Eng Manuf 2012;13(5):807–24.
[45] Sarac M, Solazzi M, Frisoli A. Design requirements of generic hand exoskeletons and survey of hand exoskeletons for rehabilitation, assistive, or haptic use. IEEE Trans Haptics 2019;12(4):400–13.
[46] Boser QA, Dawson MR, Schofield JS, Dziwenko GY, Hebert JS. Defining the design requirements for an assistive powered hand exoskeleton: A pilot explorative interview study and case series. Prosthet Orthot Int 2020;0309364620963943.
[47] Chu C-Y, Patterson RM. Soft robotic devices for hand rehabilitation and assistance: A narrative review. J Neuroeng Rehabil 2018;15(1):9.

[48] Sarakoglou I, Brygo A, Mazzanti D, Hernandez NG, Caldwell DG, Tsagarakis NG. Hexotrac: A highly under-actuated hand exoskeleton for finger tracking and force feedback. In: 2016 IEEE/RSJ international conference on intelligent robots and systems. IEEE; 2016, p. 1033–40.
[49] Wege A, Kondak K, Hommel G. Mechanical design and motion control of a hand exoskeleton for rehabilitation. In: IEEE international conference mechatronics and automation, 2005, Vol. 1. IEEE; 2005, p. 155–9.
[50] Iqbal J, Tsagarakis NG, Caldwell DG. A multi-DOF robotic exoskeleton interface for hand motion assistance. In: 2011 Annual international conference of the IEEE engineering in medicine and biology society. IEEE; 2011, p. 1575–8.
[51] Sun N, Li G, Cheng L. Design and validation of a self-aligning index finger exoskeleton for post-stroke rehabilitation. IEEE Trans Neural Syst Rehabil Eng 2021;29:1513–23.
[52] Li G, Cheng L, Sun N. Design, manipulability analysis and optimization of an index finger exoskeleton for stroke rehabilitation. Mech Mach Theory 2022;167:104526.
[53] Li G, Cheng L, Gao Z, Xia X, Jiang J. Development of an untethered adaptive thumb exoskeleton for delicate rehabilitation assistance. IEEE Trans Robot 2022;38(6):3514–29.
[54] Conti R, Meli E, Ridolfi A, Bianchi M, Governi L, Volpe Y, et al. Kinematic synthesis and testing of a new portable hand exoskeleton. Meccanica 2017;52(11–12):2873–97.
[55] Secciani N, Bianchi M, Meli E, Volpe Y, Ridolfi A. A novel application of a surface ElectroMyoGraphy-based control strategy for a hand exoskeleton system: A single-case study. Int J Adv Robot Syst 2019;16(1):1729881419828197.
[56] Secciani N, Topini A, Ridolfi A, Meli E, Allotta B. A novel point-in-polygon-based sEMG classifier for hand exoskeleton systems. IEEE Trans Neural Syst Rehabil Eng 2020.
[57] Montagnani F, Controzzi M, Cipriani C. Independent long fingers are not essential for a grasping hand. Sci Rep 2016;6:35545.
[58] Huang Y, Low K. Initial analysis and design of an assistive rehabilitation hand device with free loading and fingers motion visible to subjects. In: 2008 IEEE international conference on systems, man and cybernetics. IEEE; 2008, p. 2584–90.
[59] Burton T, Vaidyanathan R, Burgess S, Turton A, Melhuish C. Development of a parametric kinematic model of the human hand and a novel robotic exoskeleton. In: 2011 IEEE international conference on rehabilitation robotics. IEEE; 2011, p. 1–7.
[60] Desplenter T, Zhou Y, Edmonds BP, Lidka M, Goldman A, Trejos AL. Rehabilitative and assistive wearable mechatronic upper-limb devices: A review. J Rehabil Assist Technol Eng 2020;7:2055668320917870.
[61] Riddle M, MacDermid-Watts K, Holland S, MacDermid JC, Lalone E, Ferreira L. Wearable strain gauge-based technology measures manual tactile forces during the activities of daily living. J Rehabil Assist Technol Eng 2018;5:2055668318793587.
[62] Cepriá-Bernal J, Pérez-González A. Dataset of tactile signatures of the human right hand in twenty-one activities of daily living using a high spatial resolution pressure sensor. Sensors 2021;21(8):2594.
[63] Matheus K, Dollar AM. Benchmarking grasping and manipulation: Properties of the objects of daily living. In: 2010 IEEE/RSJ international conference on intelligent robots and systems. IEEE; 2010, p. 5020–7.
[64] Zong G, Pei X, Yu J, Bi S. Classification and type synthesis of 1-DOF remote center of motion mechanisms. Mech Mach Theory 2008;43(12):1585–95.
[65] Chiri A, Vitiello N, Giovacchini F, Roccella S, Vecchi F, Carrozza MC. Mechatronic design and characterization of the index finger module of a hand exoskeleton for post-stroke rehabilitation. IEEE/ASmE Trans Mechatronics 2011;17(5):884–94.
[66] Fontana M, Fabio S, Marcheschi S, Bergamasco M. Haptic hand exoskeleton for precision grasp simulation. J Mech Robot 2013;5(4).
[67] Jo I, Bae J. Design and control of a wearable and force-controllable hand exoskeleton system. Mechatronics 2017;41:90–101.
[68] Bianchi M, Fanelli F, Meli E, Ridolfi A, Vannetti F, Bianchini M, et al. Optimization-based scaling procedure for the design of fully portable hand exoskeletons. Meccanica 2018;53(11–12):3157–75.
[69] Nycz CJ, Bützer T, Lambercy O, Arata J, Fischer GS, Gassert R. Design and characterization of a lightweight and fully portable remote actuation system for use with a hand exoskeleton. IEEE Robot Autom Lett 2016;1(2):976–83.
[70] Manna SK, Dubey VN. Comparative study of actuation systems for portable upper limb exoskeletons. Med Eng Phys 2018;60:1–13.
[71] Grosu S, De Rijcke L, Grosu V, Geeroms J, Vanderboght B, Lefeber D, et al. Driving robotic exoskeletons using cable-based transmissions: A qualitative analysis and overview. Appl Mech Rev 2018;70(6).
[72] Rodriguez-Cianca D, Rodriguez-Guerrero C, Verstraten T, Jimenez-Fabian R, Vanderborght B, Lefeber D. A flexible shaft-driven remote and torsionally compliant actuator (RTCA) for wearable robots. Mechatronics 2019;59:178–88.
[73] Brogi C, Secciani N, Bartalucci L, Pagliai M, Allotta B, Ridolfi A, et al. Wearable exoskeletons for hand assistance: Concept and design of a thumb module with hybrid architecture. In: Symposium on robot design, dynamics and control. Springer; 2022, p. 70–8.
[74] Lin H-T, Kuo L-C, Liu H-Y, Wu W-L, Su F-C. The three-dimensional analysis of three thumb joints coordination in activities of daily living. Clin Biomech 2011;26(4):371–6.